Ultrasound Localization of Nitinol Wire of Sub-Wavelength Dimension

D. R. DeVries, *Student Member, IEEE*, L. J. Olafsen ⓘ, *Senior Member, IEEE*, J. S. Olafsen,
H. H. Nguyen, *Student Member, IEEE*, K. E. Schubert ⓘ, *Senior Member, IEEE*,
S. Dayawansa, and J. H. Huang

Abstract—Goal: **To enhance endovascular navigation using surgical guidewires and the use of ionizing radiation, we demonstrate a method for ultrasonic localization of wires with diameters less than the wavelength of ultrasound in the medium.** *Methods:* **Nitinol wires with diameters ranging from 50 μm to 250 μm were imaged ultrasonically in a 0.25-in-diameter water-filled tube in a gelatin medium. Imaging frequencies were 5 MHz, 7.5 MHZ, and 10 MHz.** *Results:* **For the full range of diameters traversing the phantom, the wires were localized successfully via visual inspection of both regular and difference ultrasound images. Similarly, two convolutional neural networks were trained, and both achieved an accuracy of over 95%.** *Conclusions:* **Wires with diameters as small as 50 μm were localized successfully in a water-based gelatin phantom, indicating the potential use of ultrasound to enhance endovascular navigation and surgical treatment.**

Index Terms—Ultrasound, sub-wavelength localization.

Impact Statement—Wires with diameters smaller than the ultrasound resolution wavelength in a water-based medium were localized successfully, providing a promising method for locating endovascular wires in narrow arteries without ionizing radiation.

I. Introduction

NEUROSURGEONS and interventional neuroradiologists rely on endovascular techniques to treat strokes, aneurysms, and other conditions in the brain whenever possible without drilling through the skull. Surgical wires, to guide catheters or other endovascular devices, typically are inserted at the groin and guided manually to the treatment site in the brain. Current technology for localizing the wire or catheter during insertion involves X-ray fluoroscopy [1]. This repeated illumination during a surgical procedure provides a significant radiation dose to patient and surgeon. The ability to enhance navigation as well as to replace ionizing radiation with ultrasound would reduce the exposure for the patient and cumulative exposure for the surgeon that occurs over many procedures performed. An exact reconstruction of the wire's image is not required. Locating the wire in the blood vessel roadmap generated from an initial single CT scan or X-ray is sufficient.

Ultrasound is a safe (non-ionizing), low-cost, portable, and widely available imaging modality that uses high frequency sound waves typically in the 1–10 MHz range. Lower frequencies (1–3 MHz) are used for deeper structures such as the liver or heart, and higher frequencies (5–10 MHz) are used for imaging near the skin [2].

For decades, ultrasound has been used in the localization of metal objects larger than the ultrasound wavelength in the body. There is a vast literature on ultrasound guidance for needles, particularly in sports medicine and rheumatology, where needles are used to drain fluid buildup [3], [4] or to precisely inject pain medicine or anti-inflammatories [5]–[7]. Ultrasound guidance is also used to guide catheter placement [8]–[11] and cannulation of the subclavian vein [12], [13]. Another major use of ultrasound is in marker placement and subsequent guidance, such as hook wires in breast cancer [14], [15] and fiducials in rectal cancer [16].

There have been previous studies attempting to use ultrasound for navigation in endovascular procedures [17]. In this case, they were tracking an endovascular probe in the presence of a Nitinol stent. They were not tracking a Nitinol catheter or thin wire. Nitinol stents themselves have been evaluated post-operatively via ultrasound [18], providing promise for ultrasound as a viable imaging methodology for Nitinol wire location and navigation. Nitinol is of interest in this work due to its shape-memory characteristics that make it possible to program a bend at the tip. Thus, endovascular navigation may be accomplished by current-activated heating [19].

Resolution is typically measured using the well-known Rayleigh criterion, which states the resolution is proportional to the wavelength, and true subwavelength imaging systems us evanescent waves [20]. In ultrasound, it has been noted that the

Rayleigh criterion is not always appropriate, but when speckle is involved, as it is in this case, the Rayleigh criterion is the correct criterion to use [21]. The wavelength limit of resolution using ultrasound is found by dividing the speed of sound in the medium by the ultrasound frequency. The speed of sound in water is approximately 1480 m/s and in tissue is estimated as 1540 m/s, close to the value of water due to the predominance of water content. This yields wavelengths of 300 μm at 5 MHz, 200 μm at 7.5 MHz, and 150 μm at 10 MHz. An exact image reconstruction cannot be obtained for objects with dimensions below these wavelengths.

To deliver a sensor or tool to a surgical target, localization is needed rather than a high-resolution image. The ability to differentiate the wire from the surrounding fluid or tissue is essential and often sufficient for the surgeon. In this work, we demonstrate the capability to localize Nitinol wires of sub-wavelength dimension, with sufficient pixel intensity to distinguish from the background image. To facilitate this, we introduce two neural network models, one operating off a direct ultrasound image and the other employing difference imaging. Training a neural network provides unbiased, robust verification of wire location, an important first step in establishing viability for automation of the localization process. In the future, this can be applied to implementation of robotic diagnosis and procedures and enable treatment in remote locations.

Deep learning is a subset of machine learning that uses multilayer neural networks to perform desired tasks by using trained models (see Supplementary Material). Convolutional neural networks (CNNs) are one of the most popular types of deep neural networks. A CNN consists of many layers, including a convolutional layer, a pooling layer, and a fully connected layer. Over the years, tremendous progress has been made in image recognition with CNNs and the availability of large data sets. However, training CNN from scratch requires large datasets beyond what are available in most medical imaging situations. Transfer learning helps to address the issue, as the knowledge from pre-trained models to solve one task can be transferred to accomplish another task. There are two types of transfer learning: (i) extracting features from a well-trained CNN model over a large data set of images, then adding a new separate classifier on top of the learned feature maps, and (ii) fine tuning the last layers of a pre-trained CNN model by training newly added specialized classifier layers [22]. VGG-16, developed by Simonyan and Zisserman of the Visual Geometry Group from the University of Oxford, is one of the pre-trained CNN models [23]. We employ VGG-16 in this work.

Materials and Methods are presented in Section II, followed by Results in Section III. These results are discussed in Section IV, with conclusions drawn in Section V.

II. MATERIALS AND METHODS

To illustrate the capability to locate wire position in arteries using ultrasound, gelatin phantoms were constructed to mimic tissue (Fig. 1). The gelatin phantoms were constructed by combining 1 cup of gelatin with 4 cups of water and 4 tbsp of isopropyl alcohol as a preservative. Additional details may be
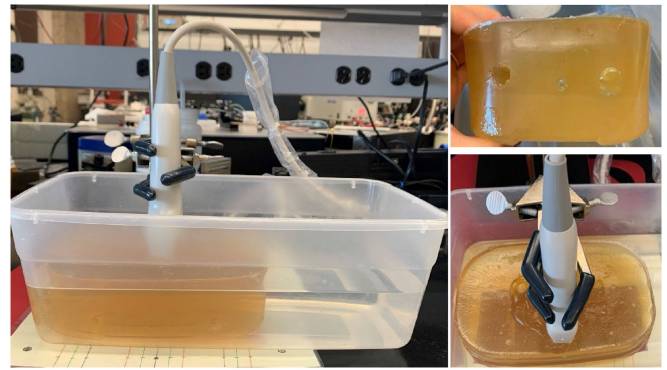

Fig. 1. Side (left) and top (bottom right) views of the ultrasound measurement system. The ultrasound probe was fixed with a clamp in the top-middle of the phantom (position C0). The tub contained enough water to fill the tubing, through which the Nitinol wires were fed at prescribed positions for ultrasonic imaging. Side view (top right) of a gelatin phantom with 0.375 in, 0.25 in, and 0.5 in diameter feedthrough tubes (left to right). 0.25 in was used exclusively for consistency.

found in [24]. Rods were inserted in the gelatin during the fabrication to create tubes that would simulate arteries (0.25 in). Just as arteries fill with blood, the phantom was partially submerged in water in a plastic tub. Care was taken to ensure the tunnels through the phantoms were filled with water without any air bubbles. The use of water is necessary as air in the tube will not transmit ultrasound waves. Water additionally is translucent, allowing visual verification of the wire location.

The ultrasound phantom was placed on a grid. The grid contained three groupings of lines: three lower (right), five central, three upper (left). These groupings represent the regions in which the wire is relatively far from the probe (lower/right), moving under the probe (center), and clearly under the probe (upper/left). The lines mark the advancement of the leading tip of the wire through the phantom, as shown in Fig. 2 from right to left. Additional images are available in the Supplementary Material. Within a grouping, the lines were separated by 0.4 in. The groups were separated by 1.2 in (i.e., the distance between U0 and C2 as well as the distance from C-2 to L0: 6 squares at 5 squares per inch). The Contec Medical Systems Company B-Ultrasound Diagnostic System, Model CMS600P2 was used to image, with center frequency of 7.5 MHz. The ultrasound linear probe (model L7.5-80L40-A16A) was placed on the phantom at the grid position C0, held by a clamp that kept the probe steady while imaging. Ultrasound gel (visible in the lower right panel of Fig. 1) was used to improve the coupling between the probe and the gelatin medium. A Nitinol wire was fed through the tunnel in the phantom starting at the right end. The tip of the wire was advanced to each line on the grid: L2 to L1, L1 to L0, L0 to C-2, and so forth. Each time the wire was advanced, an image was taken. Due to the position of the wire tip relative to the probe positioned at C0, positions U2, U1, U0, C2, C1, and C0 are identified "with wire" and C-1, C-2, L0, L1, and L2 are "without wire." Ultrasound images were collected at 5 MHz, 7.5 MHz, and 10 MHz using a linear probe. Measurements were repeated for Nitinol wires that were 20–25 cm long with diameters of 75 μm, 100 μm, 125 μm, 150 μm, and
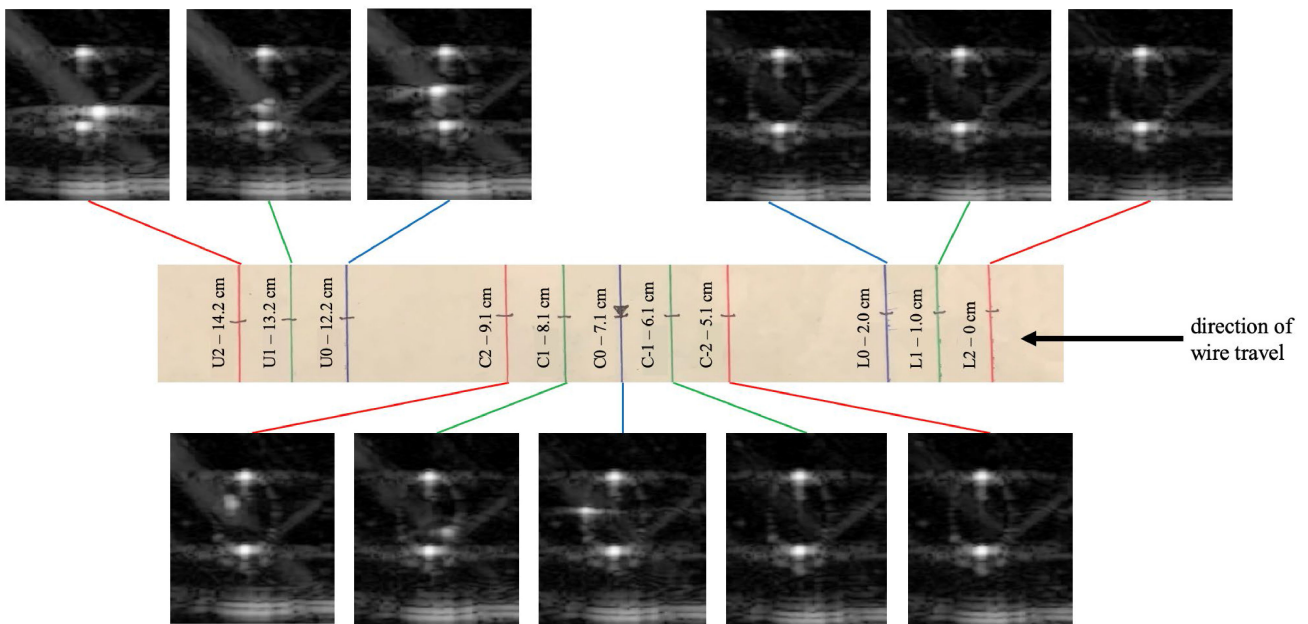
Fig. 2. Images when the tip of the wire is located at the corresponding grid locations for 75-μm-diameter wire at 7.5 MHz. The wire is inserted from right to left.

250 μm. For 50-μm-diameter wire, two sets of measurements were taken at 7.5 MHz (none at 5 MHz or 10 MHz).

For the neural network analysis, a fine tuning VGG-16 model is executed to classify the ultrasound images with and without the Nitinol wire in the feedthrough tubes of the gelatin phantom. Two data sets are examined. The first data set of 187 images (102 with wire and 85 without wire) is the original set of ultrasound images, including all six wire diameters and the three ultrasound frequencies. The second data set of 170 images (102 with wire and 68 without wire) is the set of images taking the difference between the regular image and the image at the L2 position. Each data set is split into a training set and a validation set. After importing the VGG-16 model, the three fully connected layers are discarded. Then the new specialized CNNs are trained using the gelatin phantom data sets. These specialized CNNs are small 3-layer with 3 by 3 kernels of numbers 32, 32, and 64. A regular sigmoid function is used to classify the images into two classes of with and without wire. The newly trained specialized CNN then is fed the features from the frozen VGG-16 model and the pre-trained weights are loaded into the model.

III. RESULTS

Fig. 3 displays images in which a 100-μm-diameter Nitinol wire is present in the water-filled tube for the three different imaging frequencies. Images were collected with the leading tip of the wire at U2, one of the positions for which the wire is fully under the probe. The outline of the circular tube is evident, with bright reflections at the top and bottom of the tube in each image. The third bright spot in each of the images is the wire: lower left of the tube at 5 MHz (Fig. 3(a)), on the right just below center at 7.5 MHz (Fig. 3(b)), and slightly up and to the right of the bottom reflection artifact at 10 MHz (Fig. 3(c)). Note that
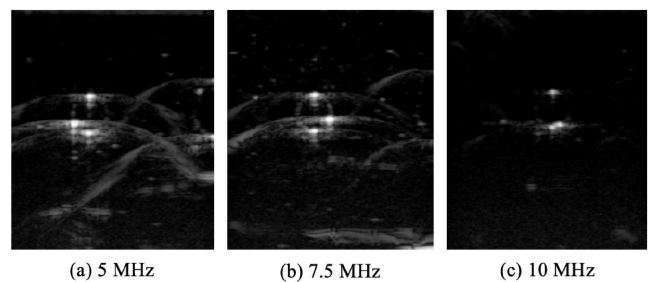

(a) 5 MHz   (b) 7.5 MHz   (c) 10 MHz

Fig. 3. Images at 5 MHz, 7.5 MHz, and 10 MHz at position U2 with a 100-μm-diameter wire Nitinol wire present in the water-filled tube.

there are more reflections and artifacts leading to larger noise background at the lower frequencies than at 10 MHz.

Images are shown in Fig. 2 at 7.5 MHz frequency as a 75-μm-diameter wire was advanced from position L2 to position U2. The ultrasound probe was fixed at position C0. Images were taken when the tip of the wire was at each of the labeled positions. All images shown are for 0.25-in-diameter tubing. At the rightmost positions (L2, L1, L0, C-2, C-1) there is no visual evidence of the presence of the wire. In the remaining images, as the wire passes under the probe fixed at position C0, there is an additional reflection indicating the presence of the wire: left for C0, lower right for C1, upper left for C2, left center for U0, bottom center for U1, and lower right for U2.

To facilitate locating the wire and distinguishing that object from other bright spots in the ultrasound images, differences were taken between images. This has the advantage of filtering out background reflections that do not correspond to the actual wire, particularly the reflections at the top and bottom of the tube. Difference images are shown in Fig. 4 for a 75-μm-diameter wire imaged at 5 MHz. The image at L2 was subtracted from
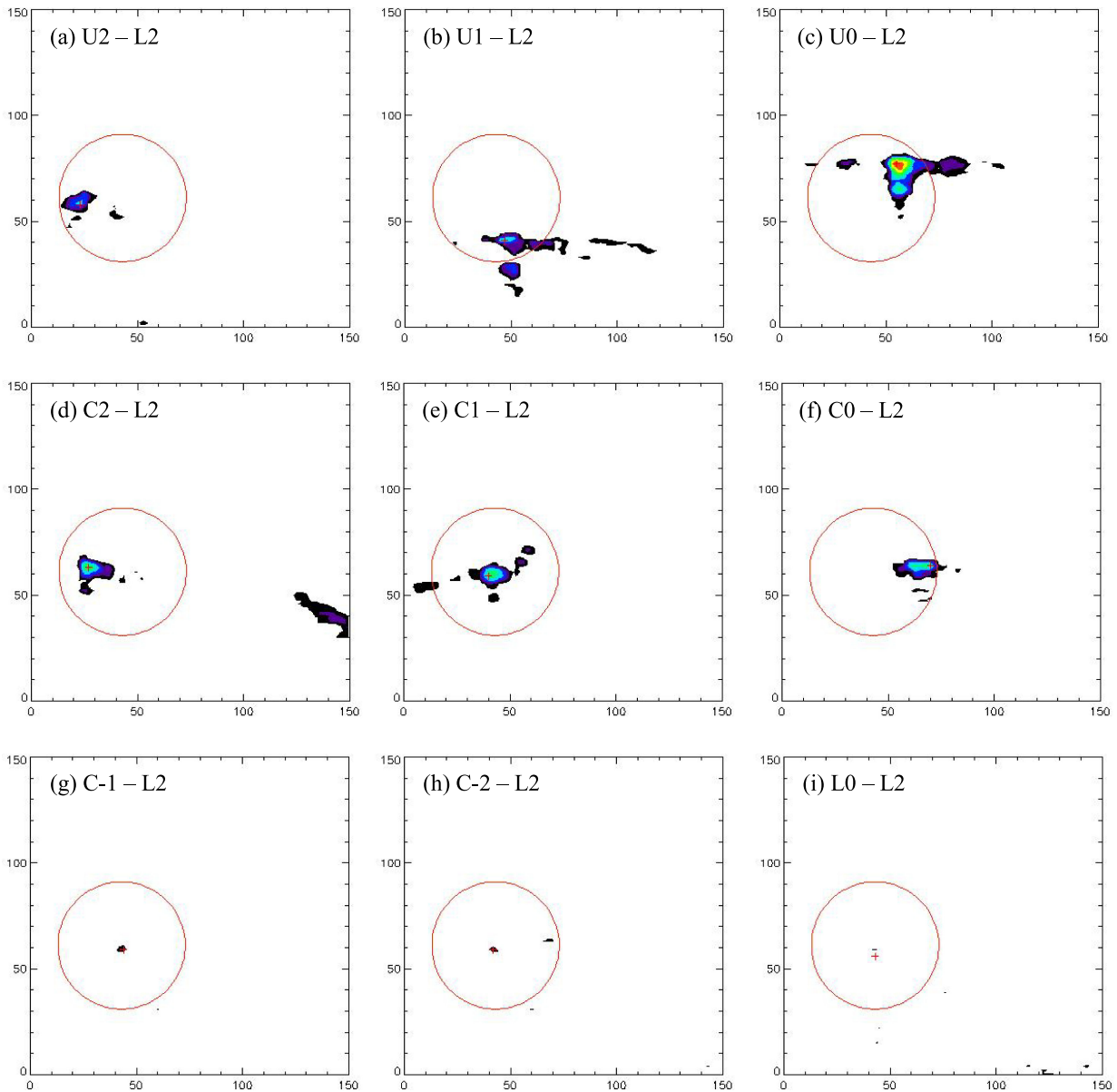
Fig. 4. Difference images for positions U2 through L0 relative to image L2 for the 75-μm-diameter wire imaged at 5 MHz. The circle was added to show the boundary of the 0.25-in-diameter water-filled tube. Horizontal and vertical axes denote the position in units of pixels. 0.25 in corresponds to 30 pixels.

the images collected at each of the other wire positions. L2 was chosen as a reference because in this image, the wire is furthest from position C0 and unlikely to generate signal in the linear probe. Note, to improve the reference in future data collection, an empty background image will be collected before the wire is introduced to the tube. The difference images indicate that the wire may begin to be distinguishable from the background at position L0, approximately 4 cm from the ultrasound transducer at C0. These images clearly locate the wire for all center and left positions.

The background fluctuations are the noise in the system. To quantify the noise, image L2 is subtracted from image L1, and the results are shown in Fig. 5a. The frames L1 and L2 were selected because the wire is farthest from the probe at these positions. The vertical axis displays the vertical position in the ultrasound image, while the horizontal axis plots the intensity difference values at each of the horizontal pixel positions along the corresponding row. Except for some initial surface reflection noise, the noise increases with depth. The larger fluctuations at the bottom (small vertical position values) relative to the top of the image correlate well with the images in Figs. 2 and 3, in which there appear to be more reflections and variation at the bottom of those images than at the top.

The peak intensity is shown in Fig. 5(b) for the difference images at each of the wire positions. Again, while visual inspection of the ultrasound images first yields evidence of the wire's position at C0, this difference analysis indicates the presence of the wire before it is directly under the ultrasonic probe. The
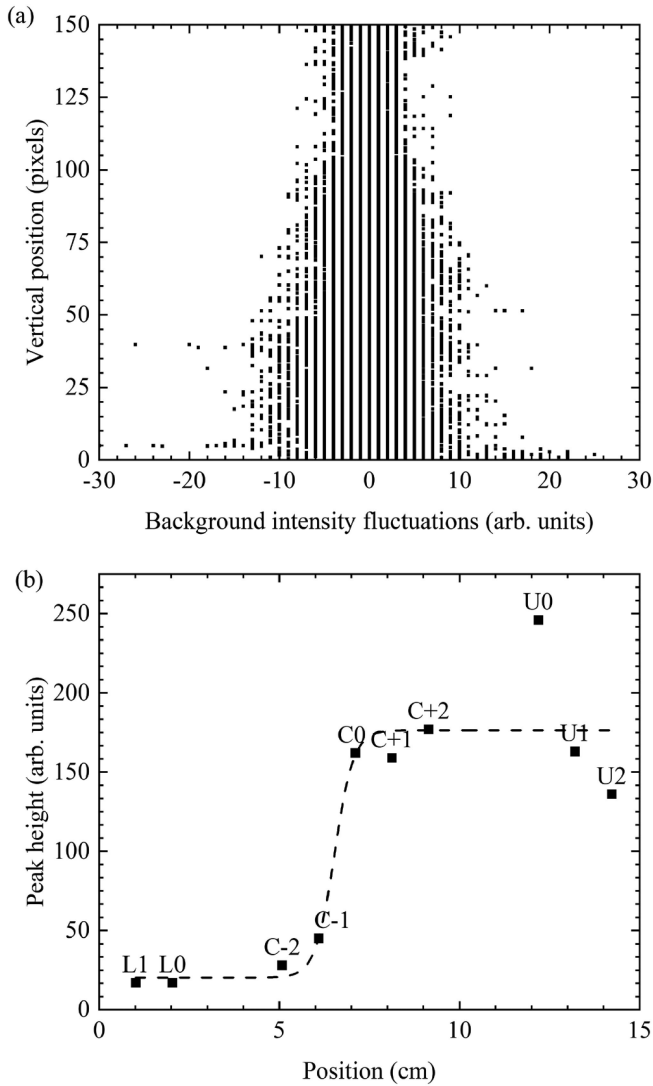
(a)

(b)

Fig. 5. (a) Background fluctuation intensities, obtained from the difference images between L1 and L2 at 5 MHz for 75-μm-diameter wire. (b) The peak pixel intensity value (of the wire) from the difference images at each position relative to L2.

dashed curve represents a Boltzmann fit to the data

$$I = A_2 + \frac{A_1 - A_2}{1 + exp(\frac{x - x_0}{dx})}, \tag{1}$$

where A_1 and A_2 are the lower and upper values of the peak height, respectively, representing the signal in different regions of the phantom. x_0 is the location of the inflection point, x is the wire location, and dx is the width of the linear portion of the slope. Note A_1 is the same level as the noise (see Fig. 5a). The ratio $A_2/A_1 = 8.7$ (19 dB) yields a measure of signal to noise in the presence of the wire.

IV. Discussion

Inspection of Fig. 4 indicates that the wire's horizontal and vertical position within the tube is changing as it is advanced down the tube. The positions of the peaks derived from the difference imaging are shown in Fig. 6, with dashed lines connecting
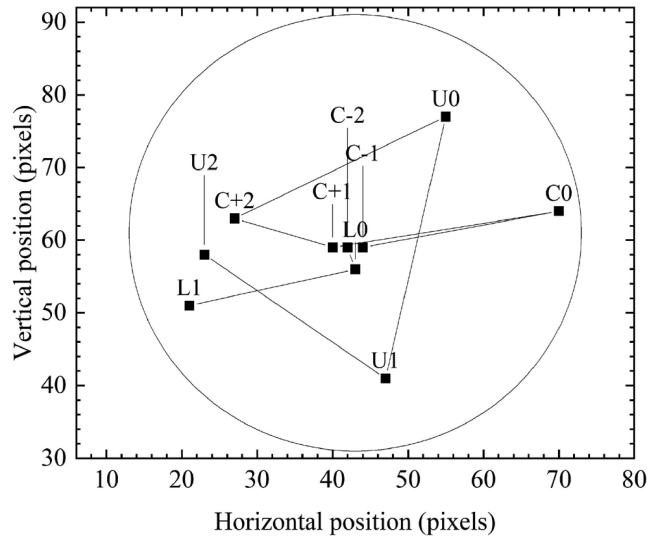

Fig. 6. The positions of the peak locations of the wire (obtained from the difference image data in Fig. 4), with the dotted line indicating the sequential progression of the wire down the tube. The circle denotes the perimeter of the tube.

consecutive measurement locations along the tube. As the wire comes into full view at C0, there is evidence that it is making a corkscrew (clockwise in Fig. 6) as it progresses further down the tube. The wire is located at its highest spot in the tube at position U0, corresponding to the largest peak height in Fig. 5b. This is understood to result from reflections at the top of the tube. The peak height is lower at U1, which is deeper in the phantom. Though it is further from the surface, it is approaching regions of high reflection at the bottom of the tube. The intensity decreases at U2 relative to U1 because the wire is farther from the top and bottom of the tube, which create strong reflections.

Visual inspection and difference imaging make it possible to identify the wire location from maximum intensities. Employing a neural network makes it possible to obtain quantifiable statements of identifiability. Results obtained from application of the CNN to the two data sets are reported in Table I. The accuracy of the method is the ratio of the correct predictions to the total number of images in the data set. The overall accuracy achieved in each of the data sets is 95.19% and 96.47%. The resulting neural networks have sensitivity, specificity, positive predictive value, and negative predictive value greater than 92%. The results from the difference image analysis are improved relative to the regular images, with respect to higher accuracy and narrower confidence intervals for accuracy, sensitivity, and positive predictive value.

There were 7 false negatives in the regular image data set and 5 false negatives in the difference image set. Three examples of each are shown in Fig. 7 (with all cases shown in Supplementary Material). For the regular image set, there were no false negatives for images taken at 10 MHz. The false negatives appear to correspond to situations in which the wire is located close to either the top or bottom strong reflection from the tubes. Even in the difference images, the overlap of the signals from the wire and strong top and bottom tube reflections seems to adversely affect the correct classification.

TABLE I
SUMMARY OF RESULTS FROM VGG-16 CNN MODEL

	REGULAR IMAGES	95% CI	DIFFERENCE IMAGES	95% CI
True Positive	95		97	
False Positive	2		1	
False Negative	7		5	
True Negative	83		67	
Accuracy	95.19%	0.9106-0.9778	96.47%	0.9248-0.9869
Sensitivity	93.14%	0.8823-0.9814	95.10%	0.90908-0.99288
Specificity	97.94%	0.9511-1.00766	98.53%	0.95668-1.0139
Positive Prediction Value	97.94%	0.9511-1.00766	98.98%	0.9699-1.00969
Negative Prediction Value	92.22%	0.86689-0.97755	93.06%	0.87184-0.98927

(a)

5 MHz 100 µm C0   5 MHz 150 µm U2   7.5 MHz 150 µm U2

(b)

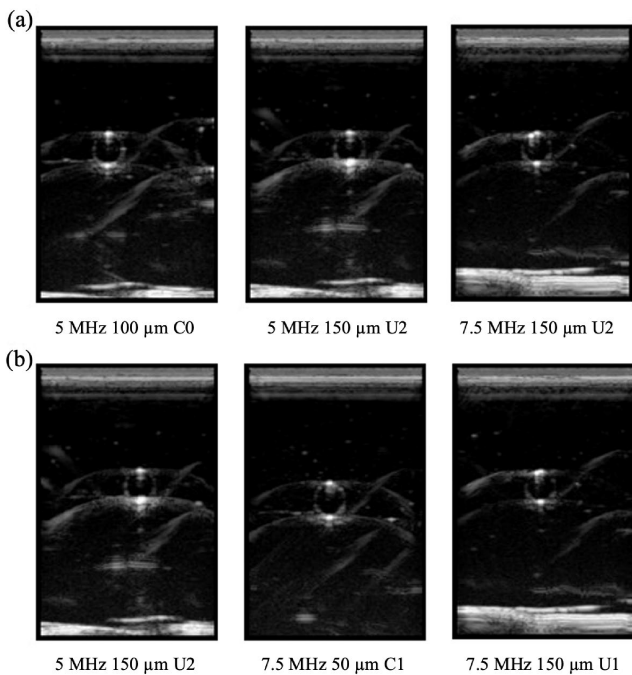5 MHz 150 µm U2   7.5 MHz 50 µm C1   7.5 MHz 150 µm U1

Fig. 7. Three examples of false negatives in the CNN analysis of (a) regular images and (b) difference images.

V. CONCLUSION

In this work, Nitinol wires in a water-filled tube in a gelatin phantom were localized successfully through analysis of ultrasound images. These diameters, ranging from 250 μm down to 50 μm, are sub-wavelength for ultrasonic frequencies in the water-based medium. Localization of sub-wavelength objects was achieved using ultrasound and enhanced by difference imaging. By subtracting the reference image with the wire furthest from the probe, the signal from the wire began to emerge from the noise while the wire tip was still as far as 4 cm away from the probe. Training and applying a CNN to both regular and difference images, 95.19% and 96.47% accuracy was achieved, respectively.

As we extend this work to include additional scattering sources, including blood cells, small bones, or other structures in tissue (cadaver or *in vivo*), the wire to be localized may not generate the maximum intensity in the image. The neural network, which would be newly trained for the more complex/*in vivo* environment, can help to identify the noise-shape envelope from the wire scatter and distinguish it from objects with higher noise fluctuations that we do not wish to identify, increasing the impact of this method. A real-time difference imaging GUI will be written easily with conventional software, leading to straightforward implementation in a surgical setting when compared to existing subwavelength imaging techniques that involve more complicated mathematical routines for image resolution. While the difference imaging gains reported here may appear to be relatively modest in the simple gelatin phantom, the benefit *in vivo* is anticipated to be more substantial when locating the wire in a system with more complex tissue structures.

Application of ultrasound and the corresponding analysis using difference imaging and neural networks for robust identification of wire location is an important first step toward a system useful to neurosurgeons and other medical professionals who rely on endovascular navigation techniques for diagnosis and treatment. Following an initial CT scan to generate a blood vessel roadmap, the surgical team would select various locations in the patient at which to verify the wire location en route to the target organ. During the surgery, the wire's exact location could be found using ultrasound as the wire is moved into view at every stage point, tracking the path of the wire to the surgical destination. Initially we would expect that the imaging would be done for mainly soft tissue (e.g., through neck soft tissue to detect the wire tip in the carotid artery). Depths will vary depending on the frequency being used and the target organ. Once the wire reaches the surgical target, a single confirmation X-ray may be taken to verify the final location of the wire tip. After fully establishing this technique, this ultrasound localization system can be used in a battlefield or other remote settings, including underdeveloped regions.

V. SUPPLEMENTARY MATERIALS

Additional figures supporting the experimental setup as well as image data are included in supplementary materials. There is a discussion of background theory of sub-wavelength localization and background discussion of machine learning, deep learning, and neural networks along with additional details about the VGG-16 algorithm.

REFERENCES

[1] B. O'Brien, F. M. Weafer, and M. S. Bruzzi, "Shape memory alloys for use in medicine," in *Comprehensive Biomaterials II, Volume I: Metallic, Ceramic, and Polymeric Biomaterials*, P. Ducheyne, K. Healy, D. W. Hutmacher, D. W. Grainger, and C. J. Kirkpatrick, Eds., Amsterdam, The Netherlands; New York, NY, USA: Elsevier, 2017, doi: 10.1016/B978-0-08-055294-1.00014-3.

[2] A. G. Webb, *Introduction to Biomedical Imaging*, Hoboken, NJ, USA: Wiley-IEEE Press, 2002.

[3] K. Raza *et al.*, "Ultrasound guidance allows accurate needle placement and aspiration from small joints in patients with early inflammatory arthritis," *Rheumatology*, vol. 42, no. 8, pp. 976–979, Aug. 2003, doi: 10.1093/rheumatology/keg269.

[4] D. Orlandi *et al.*, "Ultrasound-guided procedures around the wrist and hand: How to do," *Eur. J. Radiol.*, vol. 83, no. 7, pp. 1231–1238, Apr. 2014, doi: 10.1016/j.ejrad.2014.03.029.

[5] R. J. Finlayson, "Ultrasound guidance for trigger point injections: Gold standard or fool's gold?," *Regional Anesth. Pain Med.*, vol. 42, no. 3, pp. 279–280, Jun. 2017, doi: 10.1097/AAP.0000000000000599.

[6] D. Kumbhare *et al.*, "Ultrasound-guided interventional procedures: Myofascial trigger points with structured literature review," *Regional Anesth. Pain Med.*, vol. 42, no. 3, pp. 407–412, 2017, doi: 10.1097/AAP.0000000000000572.

[7] P. Fusco *et al.*, "Ultrasound-guided dry needling treatment of myofascial trigger points for piriformis syndrome management: A case series," *J. Chiropractic Med.*, vol. 17, no. 3, pp. 198–200, Aug. 2018, doi: 10.1016/j.jcm.2018.04.002.

[8] A. Peris, L. Tutino, G. Cianchi, and G. Gensini, "Ultrasound guidance for pleural-catheter placement," *New Engl. J. Med.*, vol. 378, no. 14, Apr. 2018, Art. no. 19, doi: 10.1056/NEJMvcm1102920.

[9] A. Sidoti *et al.*, "Ultrasound-versus landmark-guided subclavian vein catheterization: A prospective observational study from a tertiary referral hospital," *Sci. Rep.*, vol. 9, Aug. 2019, Art. no. 12248, doi: 10.1038/s41598-019-48766-1.

[10] B. Saugel, T. W. L. Scheeren, and J. Teboul, "Ultrasound-guided central venous catheter placement: A structured review and recommendations for clinical practice," *Crit. Care*, vol. 21, Aug. 2017, Art. no. 225, doi: 10.1186/s13054-017-1814-y.

[11] N. J. Soni *et al.*, "Use of ultrasound guidance for central venous catheterization: A national survey of intensivists and hospitalists," *J. Crit. Care*, vol. 36, pp. 277–283, Dec. 2016, doi: 10.1016/j.jcrc.2016.07.014.

[12] P. M. Schulman, N. S. Gerstein, M. J. Merkel, D. A. Braner, and K. Tegtmeyer, "Ultrasound-guided cannulation of the subclavian vein," *New Engl. J. Med.*, vol. 379, no. 1, Art. no. 1, Jul. 2018, doi: 10.1056/NEJMvcm1406114.

[13] T. Rezayat, J. R. Stowell, J. L. Kendall, E. Turner, J. C. Fox, and I. Barjaktarevic, "Ultrasound-guided cannulation: Time to bring subclavian central lines back," *Western J. Emerg. Med. Integrating Emerg. Care Popul. Health*, vol. 17, no. 2, pp. 216–221, Mar. 2016, doi: 10.5811/westjem.2016.1.29462.

[14] K. J. Brown, M. R. Bashir, J. A. Baker, D. S. Tyler, and E. K. Paulson, "Imaging-guided preoperative hookwire localization of nonpalpable extramammary lesions," *Vasc. Interv. Radiol. Tech. Innov.*, vol. 197, no. 3, pp. W525–W527, Sep. 2011, doi: 10.2214/AJR.10.6176.

[15] D. B. Kopans and S. DeLuca, "A modified needle-hookwire technique to simplify preoperative localization of occult breast lesions," *Radiology*, vol. 134, no. 3, pp. 781–781, Mar. 1980, doi: 10.1148/radiology.134.3.7355235.

[16] L. S. Rigter *et al.*, "EUS-guided fiducial marker placement for radiotherapy in rectal cancer: Feasibility of two placement strategies and four fiducial types," *Endoscopy Int. Open*, vol. 7, no. 11, pp. E1357–E1364, Mar. 2018, doi: 10.1055/a-0958-2148.

[17] A. E. Bond, F. A. Weaver, J. Mung, S. Han, D. Fullerton, and J. Yen, "The influence of stents on the performance of an ultrasonic navigation system for endovascular procedures," *J. Vasc. Surg.*, vol. 50, pp. 1143–1148, Nov. 2009, doi: 10.1016/j.jvs.2009.07.072.

[18] F. J. Arena and F. A. Arena, "Intravascular ultrasound evaluation of interwoven nitinol stents at implant," *J. Vasc. Med. Surg.*, vol. 1, no. 3, Sep. 2013, Art. no. 116, doi: 10.4172/2329-6925.1000116.

[19] L. J. Olafsen *et al.*, "Current-controlled Nitinol wire for improved arterial navigation," in *Proc. SPIE 10868, Adv. Biomed. Clin. Diagnostic and Surgical Guid. Syst. XVII*, Feb. 2019, Art. no. 108681E, doi: 10.1117/12.2511670.

[20] A. Neice, "Methods and limitations of subwavelength imaging," in *Advances in Imaging and Electron Physics*, P. W. Hawkes, Ed., Amsterdam, The Netherlands; New York, NY, USA: Elsevier, 2010, vol. 163, pp. 117–140, doi: 10.1016/S1076-5670(10)63003-0.

[21] D. Vilkomerson, J. Greenleaf, and V. Dutt, "Towards a resolution metric for medical ultrasonic imaging," in *Proc. IEEE Ultrasonics Symp.*, vol. 2, 1995, pp. 1405–1410.

[22] G. Ayana, D. Kokeb, and C. Se-woon, "Transfer learning in breast cancer diagnoses via ultrasound imaging," *Cancers*, vol. 13, no. 4, p. 738, 2021.

[23] K. Simonyan and A. Zisserman, "Very deep convolutional networks for large-scale image recognition," 2015. [Online]. Available: https://arxiv.org/abs/1409.1556

[24] A. C. M. Amato *et al.*, "Gelatin model for training ultrasound-guided puncture," *J. Vasc. Bras.*, vol. 14, no. 3, pp. 200–204, Sep. 2015, doi: 10.1590/1677-5449.0088.